Available online at www.sciencedirect.com

SciVerse ScienceDirect

journal homepage: www.elsevier.com/locate/he

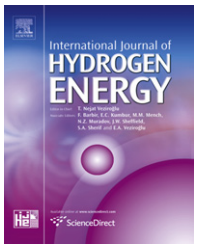

Simulation of sintering kinetics and microstructure evolution of composite solid oxide fuel cells electrodes

Yanxiang Zhang [a,b], *Changrong Xia* [a], *Meng Ni* [b,*]

[a] *CAS Key Laboratory of Materials for Energy Conversion, Department of Materials Science and Engineering, University of Science and Technology of China, Hefei, 230026 Anhui, China*

[b] *Building Energy Research Group, Department of Building and Real Estate, The Hong Kong Polytechnic University, Hung Hom, Kowloon, Hong Kong, China*

ARTICLE INFO

Article history:
Received 11 August 2011
Received in revised form
31 October 2011
Accepted 8 November 2011
Available online 16 December 2011

Keywords:
Solid oxide fuel cell
Composite electrode
Three-phase boundary (TPB)
Kinetic Monte Carlo simulation

ABSTRACT

A three-dimension (3D) kinetic Monte Carlo (kMC) model is developed to study the sintering kinetics and microstructure evolution of solid oxide fuel cell (SOFC) composite electrodes during the co-sintering processes. The model employs Lanthanum Strontium Manganite (LSM) – Yttria-stabilized Zirconia (YSZ) composites as the example electrodes but can be applied to other materials. The sintering mechanisms include surface diffusion, grain boundary migration, vacancy creation, and annihilation. A morphological dilation method is used to generate the initial LSM–YSZ compacts as the input structures for the kMC simulation. The three-phase boundary (TPB) length, porosity, and tortuosity factor of the composite cathodes are calculated during kMC sintering. Simulation results are compared with literature data and good agreement is found. Parametric study is conducted to investigate the effects of particle size, size distribution, and sintering temperature on sintering kinetics as well as the evolution of electrode microstructures. The kMC model is capable of simulating the initial and a part of intermediate sintering stages of SOFC electrodes by considering various sintering mechanisms simultaneously. It can serve as a useful tool to design and optimize the sintering processes for composite SOFC electrodes.

1. Introduction

Solid-state sintering is an indispensable process in fabricating composite electrodes of solid oxide fuel cell (SOFC) by thermally treating the ionic and electronic conducting particles to strengthen the bonding between them. A typical sintered composite electrode is shown in Fig. 1a. Prior to sintering, the powder compact is usually formed by mixing the electrode materials thoroughly with an organic slurry former, then coating onto a dense electrolyte with a thin-film technique such as screen printing [1]. Subsequently, the slurry former is burnt out in the heating stage of the sintering, leaving a porous packing of the electronic and ionic phase particles that are held together by weak surface bonds. During sintering, the bonding between particles is augmented, leading to enhancement in mechanical strength and ionic/electronic conductivities. More importantly, the sintering process creates three-phase boundaries (TPBs), where the ionic particles, electronic particles, and pores meet with each other. Since TPBs provide the sites for charge-transfer reaction, the activation polarization loss of the electrode is directly linked with the length of the TPB [2]. Apart from the TPB length, the

* *Corresponding author*. Tel.: +86 852 2766 4152; fax: +86 852 2764 5131.
E-mail addresses: bsmengni@polyu.edu.hk, memni@graduate.hku.hk (M. Ni).
0360-3199/$ – see front matter
doi:10.1016/j.ijhydene.2011.11.020

porous structures (i.e. the porosity and the tortuosity factor) influence the gas transport processes and thus contribute to the concentration polarization loss [3,4]. These basic parameters, such as TPB length, porosity and tortuosity of pores are needed input parameters in the computational fluid dynamics modeling for single cell [5,6] or cell stack optimization [7]. A high performance SOFC electrode requires efficient transport of reactant/product gases in pores, efficient transport of electrons and ions through solid structures, and large TPB length for efficient electrochemical reactions. All these are governed by the microstructures of SOFC electrodes through sintering processes.

Both experimental and mathematical modeling approaches can be employed to capture the important microstructure information of SOFC electrodes. Recently, the TPB length, the porosity, and tortuosity factor of pores are successfully extracted from the three-dimensional (3D) structures by Focused Ion Bean-Scanning Electron Microscopy (FIB-SEM) reconstruction [8–12], enabling investigation of microstructure evolution during sintering. For instance, Scott Cronin et al. [11] reconstructed the 3D microstructure of a composite Ni–Yttria-stabilized Zirconia (YSZ) anode by FIB-SEM technique. The microstructure change after 100 h sintering at 1100 °C was observed. However, the FIB-SEM technique is disadvantageous in systematically investigating the sintering kinetics, as it is complicated and time consuming. Besides, materials can be broken away during milling and phase identification procedures in SEM image processing. For comparison, mathematical modeling offers an efficient and economic way of investigating the sintering kinetics of composite electrodes of SOFC. Both analytical models and numerical approaches have been applied to simulate the sintering of SOFC electrodes, treating the electrode powders as spherical particles. In the analytical models [13–16], sintering stages are characterized by the contact angle between particles. The contact angle can vary from 15° to 90° depending on the sintering conditions, and is usually estimated from the SEM image of electrode microstructure. In the numerical models, particles are dropped within a domain to form loose particle compact with point-to-point contacts, followed by sintering simulation. For examples, Abbaspour et al. [17] modeled the sintering by enlarging particle size to obtain a certain degree of overlap between particles. In another study, Kenney et al. [18] captured the degree of sintering by varying the minimum allowable distance between contacting particles. In Metcalfe et al.'s work [19], a sintering neck is added to particle intersection region to represent the material diffusion in sintering process. These models simulate sintering from geometry perspective without the physics of sintering kinetics, i.e. without considering mass conservation.

Fully understanding the sintering kinetics of microstructure evolution is of great significance to optimize the electrode microstructure, and accordingly to improve the electrochemical performance of the cell. The kinetic Monte Carlo (kMC) models are powerful tools to simulate the 3D microstructure evolution during all sintering stages, from loose compacts to dense bulks [20–22]. However, the-state-of-the-art kMC models can only be applied for two-phase systems, such as porous single-phase compacts. In this work, we develop a kMC model to simulate the sintering of three-phase systems used for the composite SOFC electrodes. Porous Lanthanum Strontium Manganite (LSM)–YSZ composite electrodes are studied as the typical SOFC cathodes. A novel method is proposed to generate the initial LSM–YSZ particle compacts as the inputs of kMC sintering simulation. The evolution of TPB length, porosity, and tortuosity factor of pores with sintering time are calculated at different sintering temperatures, particle size, and particle size distribution of the starting materials.

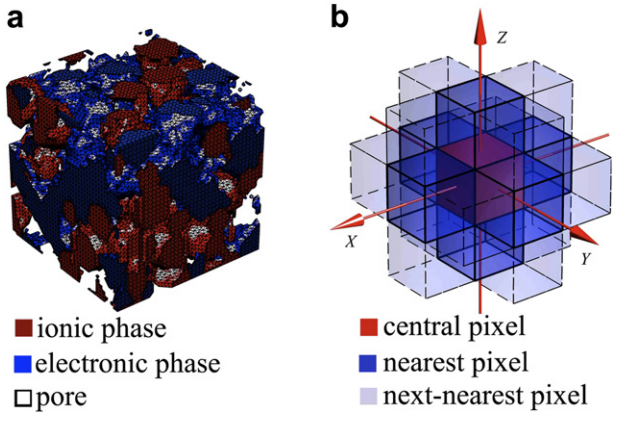

Fig. 1 – Schematics illustrating a composite electrode represented as a digitized 3D image (a), and an 18-coordinated pixel on a cubic lattice for the kinetic Monte Carlo simulation (b). The side length of one pixel is 50 nm.

2. The model

The starting powders are usually fabricated with solid-state reaction [23], co-precipitations [24], sol–gel method [25] or combustion [26]. The particles are thus micron sized or even nano-sized. So it is rational to consider each particle as a grain of the green compact. As the random-orientation of grains, the facets where they meet form grain boundaries and sintering necks. For a composite electrode shown in Fig. 1a, there are three kinds of grain boundaries/sintering necks formed by ionic–ionic, ionic–electronic, and electronic–electronic particle contacts, and two kinds of grain surfaces formed by the contacts between pores and ionic/electronic particles. The reduction of system free energy from these five kinds of interfaces is the driving force of sintering [27]. Although dislocations and point defects within grains can also contribute to free energy change, their effect is negligible and usually not considered for the solid-state sintering [28].

To calculate the system's free energy, the present kMC model discretizes the electrode structure into a digitized 3D image on a cubic lattice. The pixel is the smallest single component of the 3D image. The side length of one pixel, l, is 50 nm, which is the typical resolution of the FIB-SEM technique [8]. A pixel can represent a cubic bulk of ionic phase (e.g. YSZ), electronic phase (e.g. LSM), or pore phase by designating a pixel value, q, of a negative integer, positive integer, or zero, respectively. Each particle consists of pixels with the same and distinct pixel value to distinguish it as a unique grain different from the others. Therefore, the

system free energy can be represented by the interaction energies between pixel bulks, given by,

$$E = \frac{1}{2}\sum_{i}^{N}\sum_{j}^{n} J\left(q_i, q_j\right) w_{i,j}\left[1 - \delta\left(q_i, q_j\right)\right] \quad (1)$$

here, i is each pixel; N is the total number of pixels in the system; j is each neighbour of the pixel i; n is the total number of neighbouring pixels. The contribution of the nearest and the next-nearest neighbours are considered, as shown in Fig. 1b. The nearest and the next-nearest neighbours contribute to the surface formation and TPB formation, respectively. The effects of more distant neighbours are not included, as they are physically apart from the central pixel and do not impact the interaction energy directly. Assuming the contributions are inversely proportional to their distance from the central pixel [21], the weighting parameter, w, is then set to be 1 for the nearest neighbours and $1/\sqrt{2}$ for the next-nearest neighbours; J is the interaction energy (J) between pixel values q_i and q_j on pixel sites i and j. Its value is related to material properties and pixel volume, and cannot be determined quantitatively. However, it is reasonable to assume the value is proportional to the surface energy of the corresponding materials, due to their similar physical meanings. The surface energies of solids typically fall in a range 0.5–2 J m^{-2} [21]. But little has been reported about the SOFC materials. The YSZ-pore surface energy is estimated to be 1.4 J m^{-2} at 1100 °C [29]. To the best of our knowledge, the other four surface energies for the porous LSM–YSZ system are not available yet. According to the Back-scattered Electron images of a porous LSM–YSZ compact [30] and a composite LSM–YSZ cathode [31], the contact angles at triple junctions are the same, indicating negligible/very small difference in surface energies for various surfaces. In the present study, surface energies for various surfaces of the LSM–YSZ cathode are assumed to be the same. Thus the interaction energies of these five kinds of interfaces can be considered to be the same; δ is the Kronecker delta function with $\delta(q_i = q_j) = 1$ and $\delta(q_i \neq q_j) = 0$. Accordingly, only the interfacial energies from grain boundaries and grain surfaces are taken into account.

The energy reduction is accomplished through diffusion, grain boundary migration, and vacancy formation and annihilation. Therein, diffusion can occur in three ways: (1) evaporation–condensation diffusion; (2) bulk diffusion; (3) and surface diffusion [28]. Evaporation–condensation is a long-range diffusion, in which atoms evaporate from the grain surface with positive curvature and condense in the negative curvature region. For SOFC materials, such as LSM and YSZ, the evaporation–condensation diffusion is negligible as no LSM is observed on YSZ surface, and vice versa from sintering experiments [30]. The bulk diffusion is also neglected for the LSM–YSZ system, since the surface diffusion coefficient of oxygen is several orders higher than its bulk diffusion coefficient for LSM. For instance, the bulk diffusion coefficient is on the order of 10^{-11} cm^2 s^{-1}, while the surface diffusion coefficient is of 10^{-9} cm^2 s^{-1} at 1100 °C as extrapolated with the oxygen tracer diffusion data [32]. It is also noted that the diffusion of LSM during sintering occurs by the transport with the perovskite maintaining its stoichiometry, in other words, by transport of lattice molecules. Regarding YSZ, even surface diffusion can be neglected due to poor sintering ability of YSZ at the traditional co-sintering temperatures, e.g. 1100 °C–1200 °C. In summary, the sintering processes for composite LSM–YSZ electrodes include surface diffusion, grain boundary migration, and vacancy formation and annihilation.

Surface diffusion and grain boundary migration contribute to the growth of sintering necks. In addition, the grain boundary migration also causes grain coarsening of LSM particles. Vacancy formation and annihilation leads to compact shrinkage, accordingly affects the neck growth. To simulate these processes, the grain boundaries and surfaces should be tracked explicitly. As shown in Fig. 1b, for a central pixel representing LSM or YSZ phase, if all the nearest pixels are solid phases, and at least one of the nearest neighbours has a different pixel value with the central pixel, the central pixel is treated as a grain boundary site. If at least one of the nearest pixels is pore phase, the central pixel is then regarded as a grain surface site. In case of surface diffusion, a surface site is selected randomly, and the free energy, E_{initial} is calculated using Eq. (1). Then a random pore-phase pixel is chosen within the nearest and next-nearest neighbours of the surface site. The pixel values of the surface site and pore-phase site are exchanged, and the free energy, E_{final} is calculated. The change in energy, $\Delta E = E_{\text{initial}} - E_{\text{final}}$ is then used within the Metropolis algorithm to estimate the transition rate [33],

$$\omega_\alpha = \begin{cases} \nu_\alpha \exp(-\Delta E/kT), & \text{if } \Delta E > 0 \\ \nu_\alpha, & \text{if } \Delta E \leq 0 \end{cases} \quad (2)$$

here, α indicates LSM or YSZ phase; k is the Boltzmann constant (J/K); T is absolute temperature (K); ν is the attempt frequency which represents the inverse time of one attempt for the exchange (s^{-1}). The attempt frequency is proportional to the effective surface diffusion coefficient of sintering, $D_s = \beta l^2 \nu$, where β is a geometrical constant, l is the pixel length. To determine whether the exchange is accepted or rejected, Eq. (2) is rewritten in terms of transition probability,

$$P_\alpha = \begin{cases} \exp(-\Delta E/kT), & \text{if } \Delta E > 0 \\ 1, & \text{if } \Delta E \leq 0 \end{cases} \quad (3)$$

P_α is dimensionless, and the period it undergoes is $1/\nu_\alpha$. As discussed above, the surface diffusion of YSZ is negligible for sintering conducted below 1200 °C. That is, the period of one exchange attempt for YSZ pixels tends to be infinite. So we set $P_{YSZ} = 0$ in this work. The same Metropolis rule is also applicable for grain boundary migration. Similarly, the migration attempts of YSZ pixels are dropped. For grain boundary migration of LSM phase, a random grain boundary pixel is selected. If the grain boundary belongs to two LSM grains, the selected pixel is assigned a different value selected randomly from those of its nearest and next-nearest neighbours by a transition probability. If the grain boundary belongs to an LSM grain and a YSZ grain, the migration is rejected. In practice, LSM can react with YSZ to form a new phase, $La_2Zr_2O_7$ above 1100 °C [34]. For example, after 4 h sintering at 1200 °C, a thinly layered $La_2Zr_2O_7$ is formed with a thickness of ~45 nm. The thickness is increased to ~75 nm after 20 h sintering [35]. Since the resolution of the present kMC model is 50 nm, which is insufficient to accurately capture this phenomenon, the reaction between LSM and YSZ is not

considered. However, the reaction kinetics can be studied after the model resolution is improved to lattice scale (e.g. 0.5 nm), which is not practical to study the meso-scale structure change. In the kMC model, time is measured in units of kMC steps (kMCS). During one kMCS, all pixels of grain surfaces and boundaries have one chance to diffuse and migrate simultaneously. In addition, vacancies, defined as single pore-phase pixels surrounded entirely by nearest grain pixels, can be created during surface diffusion. Jørgensen and Mogensen showed that the density of porous LSM–YSZ electrodes is increased when the sintering temperature increased from 1150 °C to 1300 °C [36]. Tsai and Barnett showed that different porosity of LSM–YSZ composite electrodes were obtained by sintering at different temperatures, from 1100 °C to 1200 °C [37]. These results indicate an electrode shrinkage induced by sintering. In this work, once a vacancy is created, its annihilation is performed, which contributes to the compact shrinkage. Our extensive experiments at USTC show that, for the thin-layer LSM–YSZ electrode co-sintered with anode supported or electrolyte supported substrate, the electrode shrinkage only occurs in the thickness direction, while the shrinkage in the two dimensions corresponding to electrode area is not observed. This may be caused by the biaxial tension by the electrolyte [38]. Therefore, the vacancy annihilation is performed only in the thickness direction. In other words, the vacancy pixel is annihilated by moving all the grain pixels above it down by one pixel distance. It should be noted that, after sintering procedure, residual stresses may develop and warp the cell (such as cell curvature [39]) due to thermal expansion mismatch between cell components. But this is beyond the scope of the present model, which focuses on the isothermal sintering characteristics.

As discussed on Eq. (3), the period of one kMCS is the inverse attempt frequency of LSM pixels, or in inverse proportion to its surface diffusion coefficient. This can be used to scale the kMCS with the realistic time as a function of temperature, by using LSM surface diffusivities at different temperatures. Because the interaction energy cannot be determined, the dimensionless parameter, kT/J is used as the model temperature. Two sets of literature data [34,35] are used to scale the kMCS and kT/J for LSM–YSZ systems in the section of results and discussion.

3. Structure generation and parameter calculation

The powder compacts before sintering are input structures of the kMC model. In this work, spherical particles are randomly packed in a 3D domain of specified dimensions to simulate the initial compacts. In the present kMC model, the particles and domain are divided into pixels with a resolution of 50 nm. Before dropping particles, pixel values of the 3D domain are initialized to be zero, indicating an empty container. The pixels belonging to the top, bottom, and lateral domain faces serve as the container boundaries. Then the random-dropping process is conducted using a morphological dilation method [40] as shown in Fig. 2a. Firstly, the discrete particle to be dropped acts as the so-called structuring element to dilate the present domain. In other words, the center-point pixel of the structuring element travels throughout the container boundaries as well as the pixels of dropped particles (if there are particles dropped). These pixels that the structuring element does not crossover are the candidates at which the particle can be positioned. In order to make the particle stable, a pixel with the lowest coordinate is selected as the center-point position of the particle. Then a distinct pixel value of the particle is assigned to randomly represent ionic or electronic phase depending on the desired composition. This process is repeated till the domain cannot contain any additional particle. In practice, the process is stopped once the dropping has failed for 20 times. In this work, the domain size is selected to be 3 μm × 3 μm × 3 μm (or 60 pixels × 60 pixels × 60 pixels), and the volumetric ratio of LSM to YSZ is set as 50:50% for each composite structure. Fig. 2b illustrates a generated powder compact of monosized particles with 0.3 μm radius. Fig. 2c shows a compact of lognormal distributed particles with a mean radius of 0.3 μm and a standard deviation of 0.1 μm. The morphological dilation method can also simulate the packing of arbitrary-shaped particles, making it feasible to construct powder compacts using the realistic particle shapes. In this work, the LSM and YSZ particle radius ranges from 0.2 μm to 0.4 μm. Hence the domain contains hundreds of particles, and the domain-to-particle size ratio is 3.75–7.5, which is adequate to balance the simulation time and the

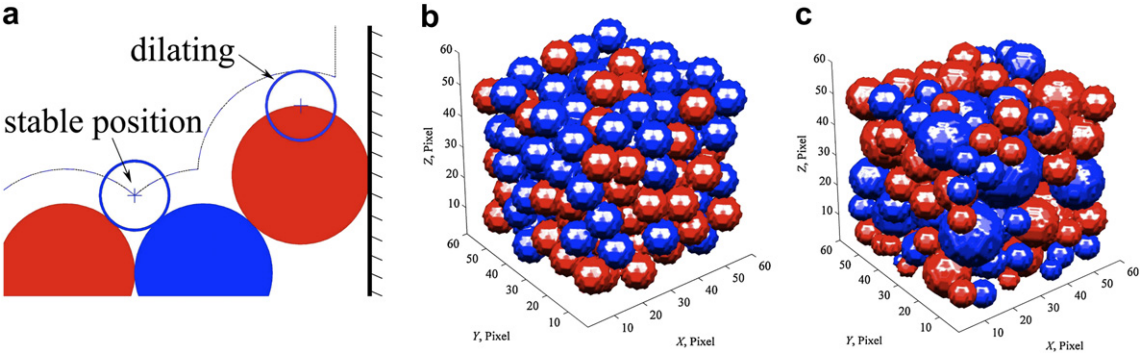

Fig. 2 – Positioning a particle by dilating the distributed particles coupled with the domain boundaries (a), and constructed 3D structures of monosized particles (b, $r_i = r_j = 0.3$ μm) and particles with a lognormal distribution (c, $r_i = r_j = 0.3$ μm, standard deviation, $\sigma = 0.1$ μm). Red colored particles are ionic phase; blue colored particles are electronic phase. (For interpretation of the references to colour in this figure legend, the reader is referred to the web version of this article.)

calculation accuracy of total TPB length, porosity, and tortuosity factor of pores. Recently, Cai et al. [41] suggest that the estimation of percolation property, such as the percolated TPB length demands a minimum domain-to-particle size ratio of 7.5. Thus the present domain size is not adequate for the percolation property calculation for particles with 0.4 μm radius. But it is big enough to calculate the general properties, such as the total TPB length, porosity, and tortuosity factor of pores. For instance, Cai et al. [41] suggest that a domain-to-particle ratio of only 2.5 is sufficient for estimating the porosity. The procedures of structure generation, kMC sintering simulation and parameter calculation are implemented in an Intel Pentium 2.4 GHz computer with a 512 MB RAM. Therein, the kMC sintering simulation is a time consuming step. The simulation time or CPU time for one kMC step simulation is dominated by the pixel amount of grain surfaces and boundaries. This is because the diffusion and migration attempts are conducted one by one, although they are considered to be simultaneous. For example, a 3 μm × 3 μm × 3 μm domain filled with 0.3 μm radius particles contains ~4.4×10^4 pixels of grain surfaces and boundaries. The CPU time for one kMC step is ~31 s. While for a 10 μm × 10 μm × 1.8 μm domain filled with 0.8 μm radius particles, there are ~1.1×10^5 grain surface and boundary pixels, and the CPU time for one kMC step is ~89 s.

Microstructure parameters in the present study include total TPB length (L_{TPB}), Porosity (φ_g), and tortuosity factor of pores (τ). During kMC sintering, the composite compact shrinks, leading to the densification. In order to capture this effect, the domain used for parameter calculation is selected as the half of the simulation domain near the bottom.

For TPB length calculation, the minimum TPB unit is identified as the pixel edge. As shown in Fig. 1b, one pixel edge is shared by four pixels. If the pixel edge is identified as a TPB unit, two conditions must be satisfied: (1) according to the definition of TPB, there must be at least an ionic pixel, an electronic pixel, and a pore-phase pixel among these four neighbouring pixels; (2) the ionic and electronic pixels must have at least two nearest neighbours of the same phase. This eliminates the error of random noise. All the TPB units configure a zig-zag series of orthogonal pixel edges. It is found that the total length of these units effectively overestimates the TPB length. To solve this problem, the total length of all TPB units is divided by a correction factor of 1.455, as proposed by Wilson et al. [10]. Note it is only applicable for 3D compacts. In the following section, the kMC model is validated using the literature data for porous LSM electrodes on YSZ electrolytes. In this case, TPBs can only be found on the 2D electrode/electrolyte interface. Accordingly, a correction factor of 1.273 should be used.

The porosity of the composite electrode can be calculated by the percentage of pore-phase pixels. Tortuosity factor of pores can be evaluated as [12],

$$\tau = \phi_g D_0 / D_{eff} \tag{4a}$$

where D_0 is the gas diffusion coefficient in free space and D_{eff} is the effective diffusion coefficient in porous media. D_{eff} can be determined by solving the Laplace's equation within the porous media,

$$\Delta\psi = 0 \tag{4b}$$

where ψ is mass concentration. Fig. 3 illustrates the calculation procedures. The boundary conditions at the bottom and top boundaries of the pore-phase subdomain are $\psi = \psi_1$ and ψ_0, respectively. No-flux conditions are applied for the lateral boundaries. Accordingly, the flux throughout the top boundary is,

$$F = -D_0 \iint \nabla\psi dadb \tag{4c}$$

Furthermore, the effective diffusion coefficient yields,

$$D_{eff}(\psi_1 - \psi_0)/c = F/(ab) \tag{4d}$$

For a given pore-phase subdomain, the ratio between diffusivities, D_0/D_{eff}, is fixed. Besides, the magnitude of ψ_1 and ψ_0 has no impact on τ calculation.

4. Results and discussion

4.1. Model validation

Two sets of literature data reported by Mitterdorfer and Gauckler [34] and Chen et al. [35] are used to scale kMCS and kT/J with the realistic sintering time and temperature, as well as to validate the kMC model. These two studies both experimentally investigated the sintering kinetics and the variation of TPB length for porous LSM electrodes on YSZ electrolytes under different conditions. In the report by Mitterdorfer and Gauckler [34], the LSM particles with a radius of about 0.1 μm were sintered at 1100 °C. In the report by Chen et al. [35], the electrode is sintered at 1200 °C but the particle size of LSM is not given. However, the radius can be easily estimated using

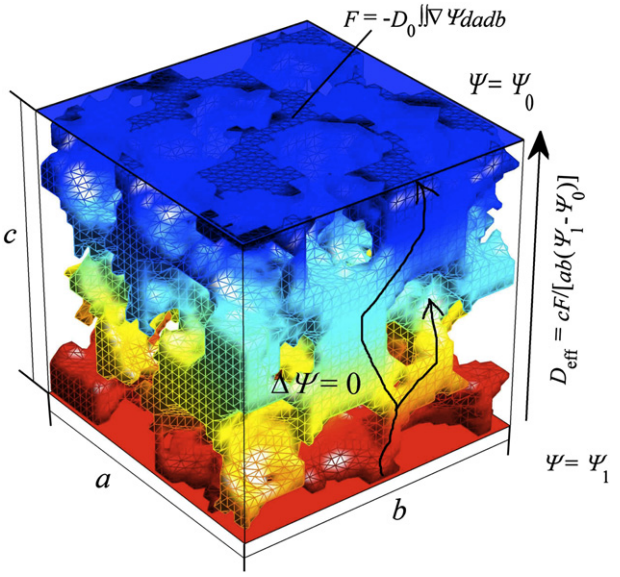

Fig. 3 – Example of tortuosity factor calculation by solving the Laplace's equation of mass concentration, Ψ, within the pore subdomain. The color from red (Ψ_1) to blue (Ψ_0) represents the solution of Ψ. For details please see the text. (For interpretation of the references to colour in this figure legend, the reader is referred to the web version of this article.)

the Film Percolation model [42]. Based on the peak TPB length, the radius is estimated to be 0.8 μm. Comparison between the simulation results and the literature data is shown in Fig. 4a and b. Because TPBs in these two reports are formed on the 2D electrode/electrolyte interface, the input structure of kMC model is simplified to a single layer compact of LSM particles with its bottom boundary in contact with YSZ electrolyte. The surface area of YSZ electrolyte is 2 μm × 2 μm when LSM particle radius is 0.1 μm, and 10 μm × 10 μm for 0.8 μm to ensure sufficient accuracy for TPB length calculation.

In the kMC simulation for the 1100 °C sintering, the TPB length is calculated as a function of model time in kMCS. The model temperature, kT/J, is varied from 0 to 3, to determine its value for 1100 °C. Note the model temperature is different from the actual sintering temperature, because kT/J depends on not only the sintering temperature (T), but also the interaction energy (J), which is a function of T. The variation of kT/J does not change the duration of one kMCS, but affects the probability of accepting changes, such as surface diffusion and grain boundary migration during one kMCS. For a given kT/J, the values of TPB length are calculated as a function of model time (kMCS). Then the model time (kMCS) corresponding to the peak TPB length is obtained. The model time is scaled by comparing the model time with the realistic sintering time of the peak TPB length. Accordingly, a series of scaling results for various kT/J values are obtained. The final scaling result is selected as the one, as it results the best agreement between simulation results and experimental data within the whole time range. As shown in Fig. 4a, good agreement is found when kT/J is 2.25. The duration of one kMCS is scaled as 90 s. 2.5 h sintering at 1100 °C is simulated in 100 kMCSs. The error-bars represent the variation range of four times simulation results, (maximum value − minimum value)/2, and the line plot is the average of the maximum and minimum values. The random error is acceptable compared with the deviation of the experimental data. The same scaling procedure is applied for sintering at 1200 °C. As shown in Fig. 4b, kT/J value is found to be 2.3, and the period of one kMCS is scaled as 30 s. 3050 kMCSs are conducted to simulate a 25.4 h sintering at 1200 °C. Only one time simulation result is shown. But its relative random error is believed to be smaller compared with that in Fig. 4a, because of its high particle-to-pixel size value [41].

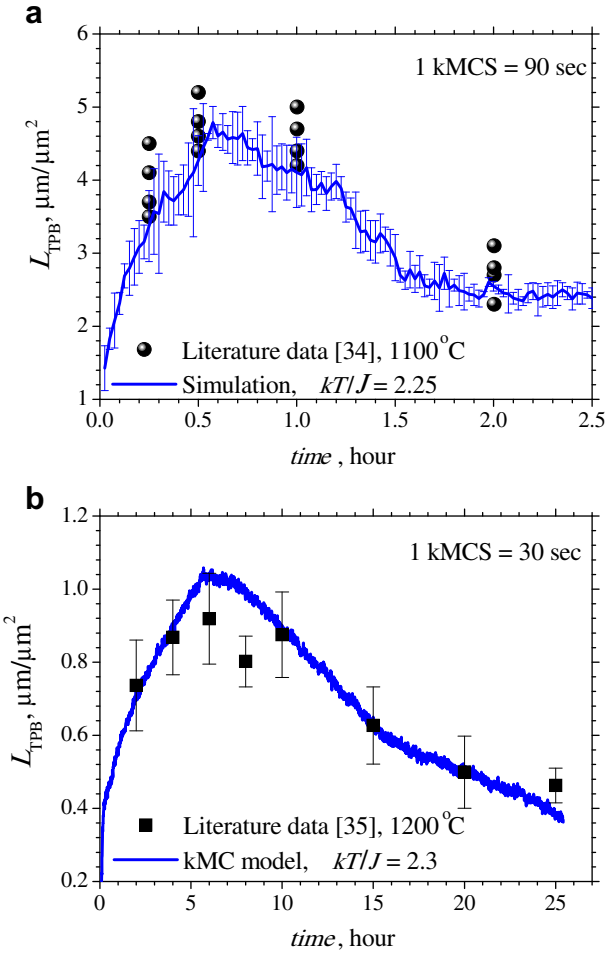

Fig. 4 – Validation of TPB length for porous LSM electrodes on YSZ electrolytes, with LSM particle radius, 0.1 μm, sintering at 1100 °C (a), and LSM particle radius, 0.8 μm, sintering at 1200 °C (b).

The scaling results of kMCS are consistent with the diffusion coefficient measurement for LSM proposed by Berenov et al. [32]. As discussed above, the duration of one kMCS is in inverse proportion to the surface diffusion coefficient. Assuming the surface diffusion thickness to be 1 nm, they reported the oxygen tracer surface diffusivities are 5.2×10^{-11} cm^2 s^{-1} at 800 °C, and 2.9×10^{-10} cm^2 s^{-1} at 900 °C. By applying Arrhenius equation, we estimate the diffusivities at 1100 °C and 1200 °C to be 4.4×10^{-9} cm^2 s^{-1} and 1.3×10^{-8} cm^2 s^{-1}, respectively. Thus, the inverse ratio of diffusivities at 1100 °C and 1200 °C is 2.9, which is close to the corresponding ratio of kMCS, 3. The good agreement between the simulation results and the literature data for these two cases validates our kMC model. In the following sections, the scaling results of kMCS and kT/J will be applied for simulating the sintering processes of composite LSM–YSZ electrodes.

4.2. *Microstructure evolution during sintering*

A green composite LSM–YSZ compact is generated using the morphological dilation method, as shown in Fig. 2b. Then the kMC simulation is performed for the sintering process at 1100 °C (kT/J = 2.25, 1 kMCS = 90 s). The snapshots of microstructures and corresponding TPB configurations at different sintering periods are shown in Fig. 5. In the initial stage of sintering, e.g. 1.25 h as shown in Fig. 5a, contacts between particles change from point-to-point type to face-to-face type. The change of contact between LSM and YSZ particles contributes to the increase in TPB length. However, the sintering necks of TPBs are still isolated from each other as shown in Fig. 5d. In this stage, the dominant process is believed to be surface diffusion due to the high absolute curvature at sintering necks [28]. After sintering for 10 h, shown in Fig. 5b, LSM particles are fully connected and their particle nature is no longer obvious. Instead, the morphology tends to be a series of interconnected solid tubes, indicating high electron conductivity. In the meantime, slight shrinkage is observed. This phenomenon is consistent with experimental observation [10]. Fig. 5e shows the TPB morphology for

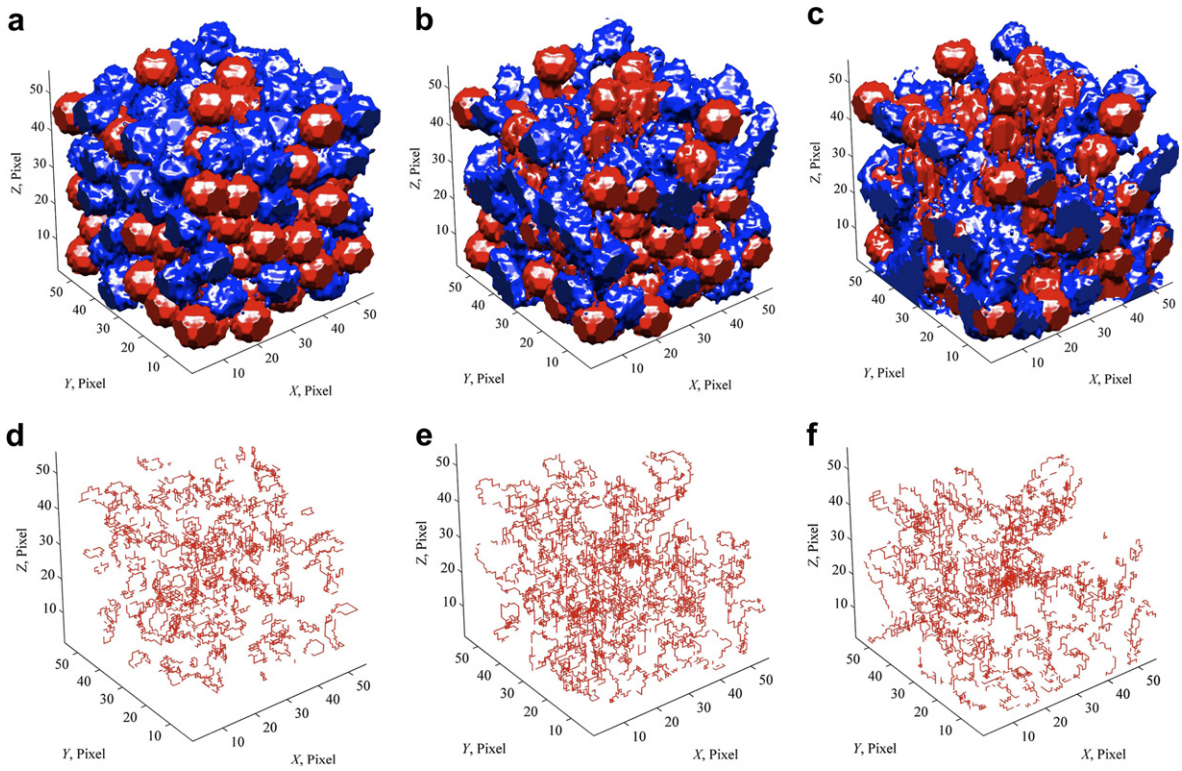

Fig. 5 – Visualization of microstructure (a, b, c) and TPB length (d, e, f) for a composite LSM–YSZ electrode ($r_i = r_j = 0.3$ μm, LSM:YSZ = 50:50 vol.%) after sintering at 1100 °C for 1.25 h (a, d), 10 h (b, e), and 20 h (c, f). Note that the domain for visualization is smaller than the simulation domain with a size, 3 μm × 3 μm × 3 μm (or 60 pixels × 60 pixels × 60 pixels).

sintering at 1100 °C for 10 h. It can be seen that the sintering necks of TPBs grow substantially and begin to fuse together. Accordingly, TPB length is further increased. While after 20 h sintering, the compact shrinkage dominates structure evolution, leading to the densification, as shown in Fig. 5c. As a result, the TPB necks are over-connected, leading to a decrease in TPB length (Fig. 5c,f). This tendency is also consistent with the literature data shown in Fig. 4.

4.3. *Effects of particle size*

Although it is believed that the sinterability increases with decreased particle size, no detailed information is available in the literature. Thus the particle radius of LSM–YSZ compacts is purposely varied from 0.2 μm, to 0.3 μm and 0.4 μm to examine the effect of particle size on sintering kinetics and microstructure evolution. Similar to the sintering of porous single-phase electrodes, an optimal sintering time corresponding to the peak TPB length is observed for composite electrodes (Fig. 6a). It is also found that the TPB length increases much faster for small particles than that for large particles in the early sintering stage. In addition, small particles lead to high TPB length, consistent with these existing models and experimental measurements [34,35,43]. However, the duration of the peak TPB length is considerably shorter for small particles than that for large particles. For instance, when particle radius is 0.2 μm, peak TPB length is achieved after 3 h sintering and remains its value till 7 h sintering. The relatively short duration time (4 h) suggest that the sintering time should be well controlled to achieve large TPB length if small particles are used. For comparison, when particle radius is 0.4 μm, the TPB length remains almost constant during the sintering time from 10 to 40 h. It should be noted that the peak TPB length is not sustained in the sintering process of single-phase electrode, as shown in Fig. 4. This is because the TPBs are formed only on the electrode/electrolyte interface in single-phase electrodes. For comparison in the sintering of composite electrodes, the duration is probably caused by the restriction of YSZ particles throughout the electrode layer.

In terms of TPB evolution, the sintering process can be divided into three stages: the increase stage before TPB necks contacts; the plateau stage caused by the combined effects of growth and contacts of TPB necks; and the decrease stage caused by the over-connection between TPB necks. It is noted that at various sintering mechanisms dominated at different sintering stages. Fig. 6b shows the TPB length in the increasing stage. As shown, the plots of $\mathrm{Log}_{10}(L_{TPB})$ vs. $\mathrm{Log}_{10}(t)$ for various particle sizes yield a straight line with a slope close to 1/7. This slope indicates that surface diffusion dominates the sintering mechanisms, as suggested by the particle-to-particle model [28]. This is in accordance with the kMC model assumptions. However, in the plateau and decrease stages, the shrinkage derived from vacancy formation and annihilation starts to affect the TPB length.

The evolution of porosity for different particle size is shown in Fig. 6c. The porosities at the beginning are about

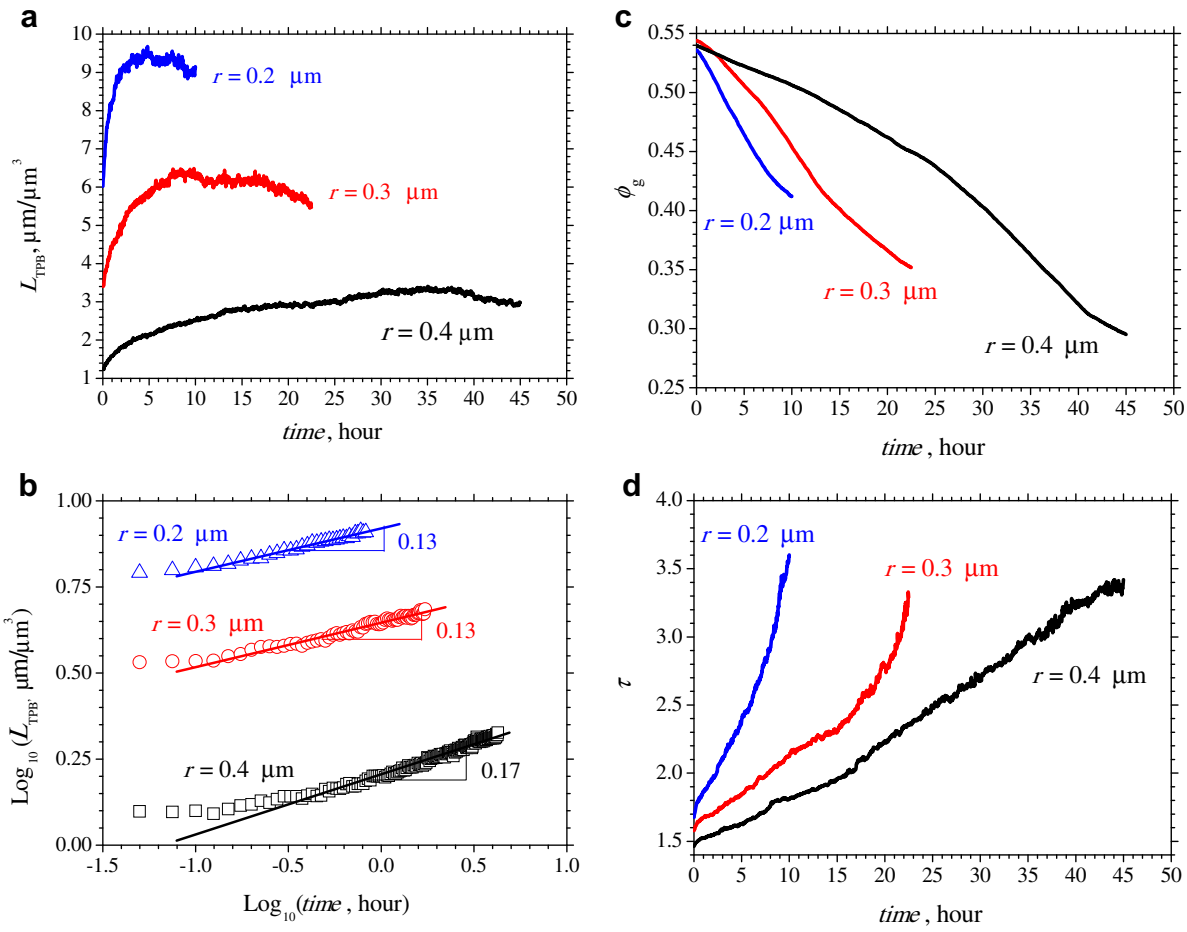

Fig. 6 – Effects of particle size on TPB formation for composite LSM–YSZ electrodes ($r_i = r_j = r$, LSM:YSZ = 50:50 vol.%) sintering at 1100 °C (a), and the logarithmic plot of TPB length vs. time in initial sintering processes (b). The evolutions of porosity and tortuosity factor of pores are shown in (c) and (d), respectively.

0.54, and decrease with the sintering time. It is also found that the porosity decrease faster for small particles. The simulated evolution curves agree well with the Makipirtti–Meng equation [44], suggesting reasonable shrinkage kinetics. With a decrease in porosity, a neck between a LSM particle and an YSZ particle has a lower probability to be exposed to pores. That is, sintering necks between LSM and YSZ particles connect with each other, and a part of the necks change into the inner grain boundaries of particle clusters. As a result, TPB length is decreased with sintering time.

According to definition of sintering stage, the shrinkage of 2–3% corresponds to the initial stage, and the intermediate stage limits the densification up to 90% before the isolation of pores occurs. According to the literature, isolated pores do not exist when porosity is higher than 0.2 [18]. So the present kMC simulations cover the initial stage and a part of intermediate stage of sintering, but the kMC can be extended to cover the other stages of sintering as well.

The evolution of tortuosity factor of pores is shown in Fig. 6d. It is found that the tortuosity factor increases with sintering time. It is believed that the increase is caused by the shrinkage in volume, which may decrease the pore size and damage the pore connectivity, even lead to isolated pores in the final stage of sintering. Due to the high sinterability of small particles, the tortuosity factor for small particles increases more drastically. It should be noted that this tendency is different from the results reported by Chen et al. [29]. In their study, a slight decrease in tortuosity factor from 3.5 to 3.2 is observed by simulating the coarsening of a composite Ni–YSZ anode at 1100 °C for 100 h. The decrease is caused by smoothing of pore surface via surface diffusion, without considering the shrinkage in their Phase-field model. As shown in Fig. 6a and d, for the same degree of sintering, tortuosity factors are almost independent of particle size. For instance, when the peak TPB length is achieved, the tortuosity factors for $r = 0.2$ μm, 0.3 μm, and 0.4 μm, are 2.3, 2.0, and 2.5, respectively. At the end of plateau stage, the tortuosity factors increase to about 3.0 for all particle sizes tested. This suggests that the beginning of plateau stage could yield the optimal structure with large TPB length and relatively small tortuosity factor.

4.4. *Effects of particle size distribution*

In practice, electrode powders usually have a particle size distribution, typically a lognormal distribution. It is thus of practical significance to study the effects of particle size

distribution on sintering kinetics. The monosized case and the polydispersed cased are shown in Fig. 2b and c, respectively, for comparison. Note the lognormal distribution of particle size is with respect to particle number, not volume. The evolution of TPB length is shown in Fig. 7a. At given sintering time, TPB length of polydispersed case is smaller than that of the monosized case. This is because the coordination number between LSM and YSZ particles is smaller for polydispersed case than that for monosized case, based on a recent theoretical analysis [16]. Despite of the difference in TPB length, the optimal sintering times to achieve the peak TPB length are the same for both cases. The same sintering kinetics is also observed for porosity evolution (Fig. 7b). The porosity for $\sigma = 0.1$ μm is smaller than that for $\sigma = 0$ μm, as polydispersed systems usually have higher packing density than the monosized systems. The evolution of tortuosity factor is shown in Fig. 7c. As can be seen, there is no obvious difference between the two cases. However, the tortuosity factor for

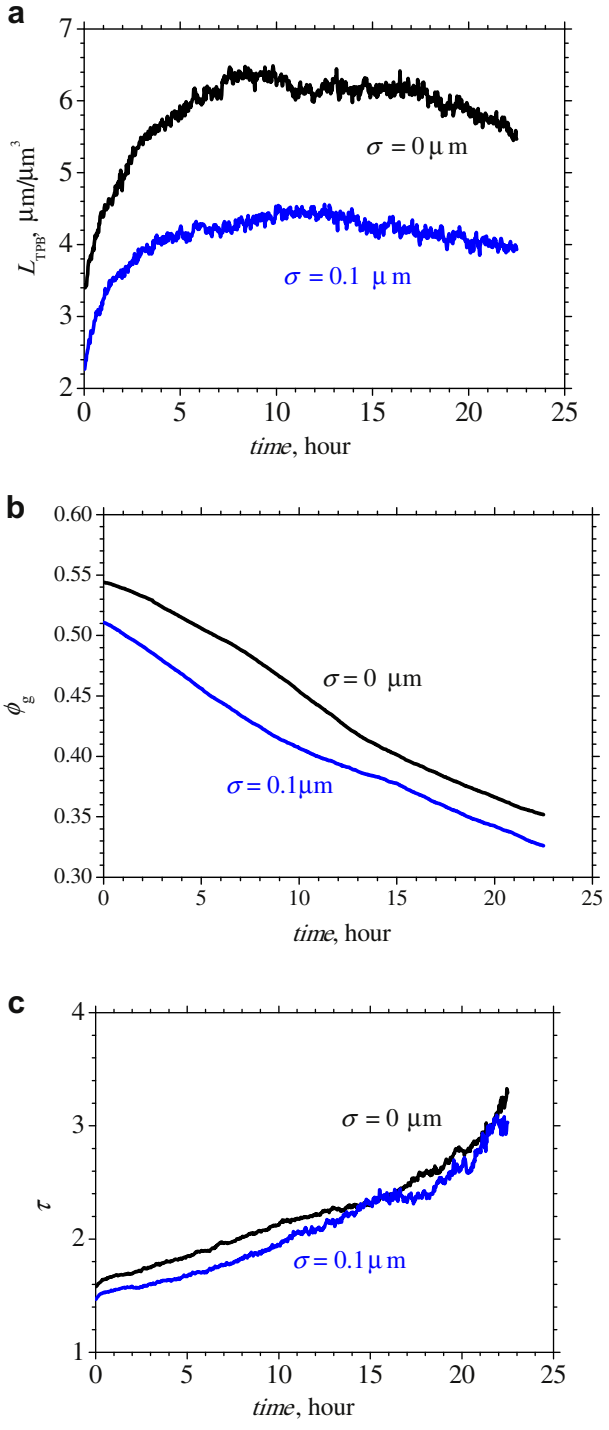

Fig. 7 – Comparison between monosized ($r_i = r_j = 0.3$ μm, standard deviation, $\sigma = 0$ μm), and lognormal distributed ($r_i = r_j = 0.3$ μm, $\sigma = 0.1$ μm) cases for composite LSM–YSZ electrodes (LSM:YSZ = 50:50 vol.%) on TPB length (a), porosity (b), and tortuosity factor of pores (c).

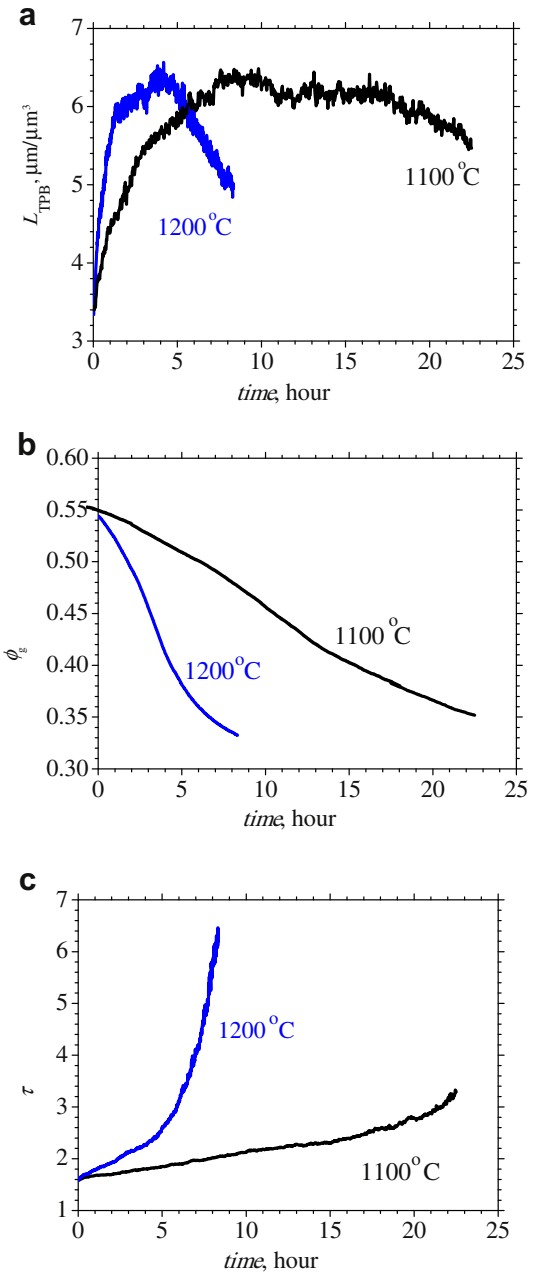

Fig. 8 – Effects of sintering temperature on TPB length (a), porosity (b), and tortuosity factor of pores (c) for a composite LSM–YSZ electrode ($r_i = r_j = 0.3$ μm, LSM:YSZ = 50:50 vol.%).

polydispersed case is slightly lower than the monosized case. The lower tortuosity factor may be caused by better pore connectivity according to the results by Kenney et al. [18]: the polydispersed case has larger mean pore size and higher percentage of large pores than the monosized case.

4.5. *Effects of sintering temperature*

During the sintering processes, temperature is the most easily controllable parameter and has substantial effect on sintering kinetics. We simulate and compare the sintering of the composite compact shown in Fig. 2b at 1100 °C ($kT/J = 2.25$, 1 kMCS = 90 s) and 1200 °C ($kT/J = 2.3$, 1 kMCS = 30 s). As shown in Fig. 8, the evolution processes of TPB length, porosity, and tortuosity factor are all accelerated when the sintering temperature is increased from 1100 °C to 1200 °C. For a given degree of sintering, such as a given TPB length, porosity, or tortuosity factor, the sintering time at 1200 °C is almost decreased to 1/3 that of 1100 °C. For example, to achieve the peak TPB length (about 6 $\mu m/\mu m^3$), 6 h is required for sintering at 1100 °C, while 2 h is enough for sintering at 1200 °C. In addition, the duration of plateau stage at 1200 °C is much shorter than at 1100 °C. Therefore, when small particles are sintered at a high temperature, careful control of sintering time is required.

The above analyses provided detailed information on the sintering of composite LSM–YSZ electrodes at typical sintering temperatures between 1100 °C and 1200 °C. They are useful for understanding the sintering kinetics so as to optimize the sintering conditions for SOFC performance improvement. For SOFC in operation at typical temperatures of about 800 °C–1000 °C, sintering can also occur and affect the long-term performance stability. According to a study conducted by Jiang and Wang [45], the sintering kinetics of SOFC electrodes in operation are quite different from those in sintering for electrode fabrication. This is because the polarization current may cause lattice expansion or shrinkage as well as the stoichiometric change, further affects the sinterability. However, the thermally induced sintering considered in this work is the most basic issue about electrode durability. The polarization effects will be included in the kMC model to predict the long-term stability of SOFC electrodes in operation in a subsequent study.

5. Conclusion

A kMC model is combined with a morphological dilation method to study the sintering kinetics and microstructure evolution of composite LSM–YSZ electrodes. The model is validated by comparing the simulation results with the experimental data from the literature. Microstructure parameters, such as TPB length, porosity, and tortuosity factor of pores are calculated during kMC sintering. The following conclusions can be obtained:

(1) The evolution of TPB length can be divided into three sintering stages – increase, plateau, and decrease stages. This suggests that the peak TPB length can be achieved by controlling the sintering time at an optimal value or in an optimal range.
(2) Different from the existing study using the Phase-field model, the tortuosity factor of pores is found to increase with sintering time, due to the compact shrinkage. Porosity is found to decrease with increasing sintering time.
(3) Small particle size leads to high sinterability. The evolutions of TPB length, porosity, and tortuosity factor of pores are faster for small particles than for large particles. In addition, high TPB length can be obtained using small particles. However, the duration of peak TPB length is shorter for smaller particles, requiring careful control of sintering time.
(4) When particle size has a distribution, the sintering kinetics is the same with that of the monosized case, i.e. the optimal sintering time does not change. However, the TPB length is lower for polydispersed particles than that of monosized particles.
(5) When sintering temperature is increased, the sintering process is facilitated. For a given sintering degree, the sintering time is shortened by a certain factor.

Acknowledgments

This research was supported by a grant from The Hong Kong Polytechnic University (Project No. A-PK48), Hong Kong and the Ministry of Science and Technology of China (2012CB215403).

REFERENCES

[1] Xia CR, Chen FL, Liu ML. Reduced-temperature solid oxide fuel cell fabricated by screen printing. Electrochemical and Solid State Letters 2001;4:A52–4.
[2] Adler SB. Factors governing oxygen reduction in solid oxide fuel cell cathodes. Chemical Reviews 2004;104:4791–843.
[3] Kim JW, Virkar AV, Fung KZ, Mehta K, Singhal SC. Polarization effects in intermediate temperature, anode-supported solid oxide fuel cells. Journal of the Electrochemical Society 1999; 146:69–78.
[4] Grew KN, Joshi AS, Peracchio AA, Chiu WKS. Pore-scale investigation of mass transport and electrochemistry in a solid oxide fuel cell anode. Journal of Power Sources 2010; 195:2331–45.
[5] Ho TX, Kosinski P, Hoffmann AC, Vik A. Numerical analysis of a planar anode-supported SOFC with composite electrodes. International Journal of Hydrogen Energy 2009;34:3488–99.
[6] Akhtar N, Decent SP, Loghin D, Kendall K. A three-dimensional numerical model of a single-chamber solid oxide fuel cell. International Journal of Hydrogen Energy 2009;34:8645–63.
[7] Chan SH, Ho HK, Tian Y. Multi-level modeling of SOFC-gas turbine hybrid system. International Journal of Hydrogen Energy 2003;28:889–900.
[8] Wilson JR, Kobsiriphat W, Mendoza R, Chen HY, Hiller JM, Miller DJ, et al. Three-dimensional reconstruction of a solid oxide fuel cell anode. Nature Materials 2006;5:541–4.
[9] Shearing PR, Golbert J, Chater RJ, Brandon NP. 3D reconstruction of SOFC anodes using a focused ion beam lift-out technique. Chemical Engineering Science 2009;64:3928–33.

[10] Wilson JR, Cronin JS, Duong AT, Rukes S, Chen HY, Thornton K, et al. Effect of composition of ($La_{0.8}Sr_{0.2}MnO_3$–Y_2O_3-stabilized ZrO_2) cathodes: correlating three-dimensional microstructure and polarization resistance. Journal of Power Sources 2010;195:1829–40.
[11] Cronin JS, Wilson JR, Barnett SA. Impact of pore microstructure evolution on polarization resistance of Ni–Yittria-stabilized zirconia fuel cell anodes. Journal of Power Sources 2011;196:2640–3.
[12] Iwai H, Shikazono N, Matsui T, Teshima H, Kishimoto M, Kishida R, et al. Quantification of SOFC anode microstructure based on dual beam FIB-SEM technique. Journal of Power Sources 2010;195:955–61.
[13] Costamagna P, Costa P, Antonucci V. Micro-modeling of solid oxide fuel cell electrodes. Electrochimica Acta 1998;43:375–94.
[14] Zhu W, Ding D, Xia CR. Enhancement in three-phase boundary of SOFC electrodes by an ion impregnation method: a modeling comparison. Electrochemical and Solid State Letters 2008;11:B83–6.
[15] Shah M, Nicholas JD, Barnett SA. Prediction of infiltrated solid oxide fuel cell cathode polarization resistance. Electrochemistry Communications 2009;11:2–5.
[16] Zhang YX, Wang YL, Wang Y, Chen FL, Xia CR. Random-packing model for solid oxide fuel cell electrodes with particle size distributions. Journal of Power Sources 2011;196:1983–91.
[17] Abbaspour A, Luo JL, Nandakumar K. Three-dimensional random resistor-network model for solid oxide fuel cell composite electrodes. Electrochimica Acta 2010;55:3944–50.
[18] Kenney B, Valdmanis M, Baker C, Pharoah JG, Karan K. Computation of TPB length, surface area and pore size from numerical reconstruction of composite solid oxide fuel cell electrodes. Journal of Power Sources 2009;189:1051–9.
[19] Metcalfe C, Kesler O, Rivard T, Gitzhofer F, Abatzoglou N. Connected three-phase boundary length evaluation in modeled sintered composite solid oxide fuel cell electrodes. Journal of the Electrochemical Society 2010;157:B1326–35.
[20] Tikare V, Braginsky M, Bouvard D, Vagnon A. Numerical simulation of microstructural evolution during sintering at the mesoscale in a 3D powder compact. Computational Materials Science 2010;48:317–25.
[21] Qiu FL, Egerton TA, Cooper IL. Monte Carlo simulation of nano-particle sintering. Powder Technology 2008;182:42–50.
[22] Fang B, Huang C, Liu HL, Xu CH, Sun S. Monte Carlo simulation of grain-microstructure evolution in two-phase ceramic tool materials. Journal of Materials Processing Technology 2009;209:4568–72.
[23] Leng YJ, Chan SH, Jiang SP, Khor KA. Low-temperature SOFC with thin film GDC electrolyte prepared in situ by solid-state reaction. Solid State Ionics 2004;170:9–15.
[24] Fang XH, Zhu GY, Xia CR, Liu XQ, Meng GY. Synthesis and properties of Ni-SDC cermets for IT-SOFC anode by co-precipitation. Solid State Ionics 2004;168:31–6.
[25] Gaudon M, Laberty-Robert C, Ansart F, Stevens P, Rousset A. Preparation and characterization of $La_{1-x}Sr_xMnO_{3+\delta}$ ($0 \leq x \leq 0.6$) powder by sol–gel processing. Solid State Sciences 2002;4:125–33.
[26] Ringuede A, Labrincha JA, Frade JR. A combustion synthesis method to obtain alternative cermet materials for SOFC anodes. Solid State Ionics 2001;141:549–57.
[27] Kang SJL. Sintering processes. In: Sintering. Oxford: Butterworth-Heinemann; 2005. p. 3–8.
[28] Kang SJL. Initial stage sintering. In: Sintering. Oxford: Butterworth-Heinemann; 2005. p. 39–55.
[29] Chen HY, Yu HC, Cronin JS, Wilson JR, Barnett SA, Thornton K. Simulation of coarsening in three-phase solid oxide fuel cell anodes. Journal of Power Sources 2011;196:1333–7.
[30] Sahu AK, Ghosh A, Suri AK, Sengupta P, Bhanumurthy K. Studies on chemical compatibility of lanthanum strontium manganite with yttria-stabilized zirconia. Materials Letters 2004;58:3332–6.
[31] Dillon SJ, Helmick L, Miller HM, Wilson L, Gemman R, Petrova RV, et al. The orientation distributions of lines, surfaces, and interfaces around three-phase boundaries in solid oxide fuel cell cathodes, Journal of the American Ceramic Society, doi:10.1111/j.1551-2916.2011.04673.x.
[32] Berenov AV, MacManus-Driscoll JL, Kilner JA. Oxygen tracer diffusion in undoped lanthanum manganites. Solid State Ionics 1999;122:41–9.
[33] Ala-Nissila T, Ying SC. Theory of classical surface diffusion. Progress in Surface Science 1992;39:227–323.
[34] Mitterdorfer A, Gauckler LJ. $La_2Zr_2O_7$ formation and oxygen reduction kinetics of the $La_{0.85}Sr_{0.15}MnyO_3$, O_2(g) YSZ system. Solid State Ionics 1998;111:185–218.
[35] Chen A, Smith JR, Duncan KL, DeHoff RT, Jones KS, Wachsman ED. Effect of $La_2Zr_2O_7$ on interfacial resistance in solid oxide fuel cells. Journal of the Electrochemical Society 2010;157:B1624–8.
[36] Jørgensen MJ, Primdahl S, Bagger C, Mogensen M. Effect of sintering temperature on microstructure and performance of LSM-YSZ composite cathodes. Solid State Ionics 2001;139:1–11.
[37] Tsai T, Barnett SA. Effect of LSM–YSZ cathode on thin-electrolyte solid oxide fuel cell performance. Solid State Ionics 1997;93:207–17.
[38] Green DJ, Guillon O, Rödel J. Constrained sintering: a delicate balance of scales. Journal of the European Ceramic Society 2008;28:1451–66.
[39] He CR, Wang WG, Wang J, Xue Y. Effect of alumina on the curvature, Young's modulus, thermal expansion coefficient and residual stress of planar solid oxide fuel cells. Journal of Power Sources 2011;196:7639–44.
[40] Gonzalez RC, Woods RE, Eddins SL. Dilation and erosion. In: Digital image processing using Matlab. New Jersey: Person Education; 2004. p. 337–47.
[41] Cai Q, Adjiman CS, Brandon NP. Modelling the 3D microstructure and performance of solid oxide fuel cell electrodes: computational parameters. Electrochimica Acta 2011;56:5804–14.
[42] Zhang YX, Xia CR. Film percolation for composite electrodes of solid oxide fuel cells. Electrochimica Acta 2011;56:4763–9.
[43] Zhang YX, Xia CR. A particle-layer model for solid oxide fuel cell cathodes with different structures. Journal of Power Sources 2010;195:4206–12.
[44] Zhang XB, Liu XQ, Meng GY. Sintering kinetics of porous ceramics from natural diatomite. Journal of the American Ceramic Society 2005;88:1826–30.
[45] Jiang SP, Wang W. Sintering and grain growth of (La, Sr)MnO_3 electrodes of solid oxide fuel cells under polarization. Solid State Ionics 2005;176:1185–91.